Contents list available at CBIORE journal website

International Journal of Renewable Energy Development

Journal homepage: https://ijred.cbiore.id

Research Article

Development of WO_3/TiO_2-NT/Ti photoanode for simultaneously POME degradation, electricity generation, and hydrogen production in a photocatalysis-fuel cell system

M. Febriansyah Bachri[a], Saddam Husein[a,c], Bambang Heru Susanto[a], Ratnawati[b], Slamet[a*]

[a]*Department of Chemical Engineering, Faculty of Engineering, Universitas Indonesia, Depok 16424, Indonesia*

[b]*Department of Chemical Engineering, Institut Teknologi Indonesia, Tangerang Selatan 15314, Indonesia*

[c]*Department of Pharmacy, Faculty of Health Science, Universitas Malahayati, Lampung 35152, Indonesia*

Abstract. This research presents a WO_3/TiO_2-NT/Ti photoanode for processing POME waste as well as producing electricity and hydrogen simultaneously. The photoanode in the form of nanocomposites was synthesized using an in-situ anodization method and characterized using Field Emission Scanning Electron Microscopy with Energy Dispersive X-ray (FESEM-EDX), X-ray Diffraction (XRD), Photoluminescence Spectroscopy (PL-Spectra), photocurrent transient, X-ray Photoelectron Spectroscopy (XPS), and UV-Visible Diffuse Reflectance Spectroscopy (UV-Vis DRS). The results showed that the WO_3/TiO_2-NT/Ti photoanode with 0.3 g of WO_3 precursor added during anodization exhibited the best PFC performance. The system achieved a COD degradation of 84%, hydrogen production of 11.18 mmol/m², and a maximum power density of 0.0375 mW/cm² under visible light irradiation, outperforming the variations with 0.5 g and 0.78 g WO_3 precursor. The enhanced performance was attributed to the formation of a heterojunction between WO_3 and TiO_2, as confirmed by characterization results and performance tests in COD degradation, electricity generation, and hydrogen production. Meanwhile, the addition of 0.5 g and 0.78 g WO_3 precursor reduced photocatalytic performance, likely due to excessive $Na_2WO_4 \cdot 2H_2O$ during anodization, which could partially cover the active TiO_2-NT/Ti surface and alter the electrochemical oxidation process. The developed WO_3/TiO_2-NT/Ti photoanode offers a promising solution for simultaneous wastewater treatment, clean hydrogen production, and electricity generation, with potential applications in sustainable palm oil processing industries and future renewable energy technologies.

Keywords: Electricity Generation, Hydrogen Production, Palm Oil Mill Effluent (POME), Photocatalysis-Fuel Cell, WO_3/TiO_2-NT/Ti Photoanode

Received: 20th Dec 2024; Revised: 17th January 2025; Accepted: 26th Feb 2025; Available online: 7th March 2025

1. Introduction

Palm Oil Mill Effluent (POME) is increasing along with a rise in the palm oil processing industries in Indonesia. Approximately 5.0–5.7 tons of water are required to generate 1 ton of crude palm (Kamyab *et al*., 2018). This process generate large POME, posing a significant health concern due to the high concentration of organic matter (16,000–50,000 mg/L COD) (Madaki & Seng, 2013; Tabassum *et al*., 2015). For POME treatment, several methods have been explored including anaerobic digestion (Tan *et al*., 2018), advanced oxidation processes (Thanekar *et al*., 2020), photocatalytic treatment (Alhaji *et al*., 2016), and anaerobic oxidation (Puyol *et al*., 2017). Compared to others, photocatalytic treatment is faster and more efficient than commonly used biological methods. Existing POME treatment focuses only on waste management without generating valuable by-products. Therefore, this research aimed to develop POME degradation system that combines photocatalysis and fuel cell technology to degrade organic compounds in POME as well as simultaneously produce electricity and hydrogen.

As an advanced photocatalysis treatment method, Photocatalysis-Fuel Cell (PFC) system is generates electricity through electron transfer during organic compound degradation (He *et al*., 2022; Lianos, 2017; Ong *et al*., 2019). The system uses semiconductor materials as photoelectrodes activated by light, consisting of photoanode and photocathode connected through an external circuit. According to (Lui *et al*., 2019), photoanode function as strong oxidizing electrode for organic waste degradation, while the photocathode accepts electrons to produce electricity. The semiconductors used in PFC system are divided into n-type and p-type, serving as the photoanode and photocathode, respectively (Z. Wang *et al*., 2021).

The selection of photoelectrodes is essential for the efficiency of the PFC system. In single photoelectrode system where only anode is illuminated, common photoanodes include TiO_2/Ti, ZnO, and TNA/Ti, with Pt often used as the cathode. Meanwhile, in dual photoelectrode systems where both anode and cathode are illuminated, photoanode-photocathode combinations such as TiO_2/Ti-Cu_2O/Cu, WO_3/W-Cu_2O/Cu, and g-C_3N_4/Fe/TiO_2-WO_3 are used (He *et al*., 2022). Dual

* Corresponding author
Email: slamet@che.ui.ac.id (Slamet)

https://doi.org/10.61435/ijred.2025.60978
ISSN: 2252-4940/© 2025.The Author(s). Published by CBIORE

photoelectrode systems offer advantages such as better light harvesting, higher charge transfer rates, and lower charge recombination (Vasseghian *et al*., 2020).

Recent research on photoanode materials for PFC systems has focused on improving both degradation efficiency and electricity generation. Chen *et al*., (2012) used a WO_3/W photoanode, achieving degradation efficiency of 58%, 63%, and 74% for phenol, rhodamine B, and Congo red, respectively, after 5 hours of illumination. Lee *et al*., (2016) applied a ZnO/Zn photoanode for reactive green 19 degradation, achieving 100% decolorization and 92% mineralization at a 10 mg/L dye concentration, with a peak power density of 1.2696 mW/cm². Furthermore, Xia *et al*., (2016) used a $BiVO_4$/WO_3/W photoanode in PFC systems, obtaining a current density of 0.0002 W/cm² in tetracycline hydrochloride degradation. J. Li *et al*., (2013) showed the effectiveness of TiO_2/Ti photoanodes for methyl orange, methylene blue, and congo red degradation, with efficiencies of 67%, 87%, and 83%, respectively. Maximum current density and power density were 0.23 mA/cm² and 0.00036 W/cm², respectively.

The combination of photoanode-photocathode in PFC system has only used ZnO/Zn-Pt (Moksin *et al*., 2021) and TiO_2/ZnO/Zn-TiO_2/CuO/Cu (Kee *et al*., 2020) for POME treatment and electricity generation. However, ZnO/Zn is unstable and less responsive to visible light. This limits the potential for solar applications and remains costly due to Pt usage. Titanium dioxide (TiO_2) has been extensively developed as a photoanode for PFC systems and remains a primary option due to low cost, environmental friendliness, and chemical stability. TiO_2 can also be synthesized as nanotubes (NT), showing more efficient photocatalytic activity compared to regular TiO_2 (Kustiningsih *et al*., 2023). WO_3 has been widely investigated for its strong oxidation power and visible light responsiveness, which enhances the potential for PFC systems to operate effectively under sunlight (Mahadik *et al*., 2023). Despite these advancements, research on photocatalysis-fuel cell (PFC) has focused on the degradation of organic compounds and electricity generation, without investigating hydrogen production.

TiO_2 on titanium (Ti) substrates is widely used due to the photocatalytic properties and chemical stability. However, the limited visible-light responsiveness of TiO_2 due to large bandgap, shows the need for improvements. In this context, WO_3 is a promising semiconductor for enhancing the performance of TiO_2. The visible-light responsiveness and more positive valence band position help to oxidize water and organic compounds more effectively. The WO_3/TiO_2 composite has been extensively studied as an efficient photocatalyst for degrading organic pollutants in water, using UV and visible light spectra (Luo *et al*., 2013; Mokhtarifar *et al*., 2020). However, the application as a photoanode in electrochemical systems remains underexplored, presenting opportunities for future multifunctional developments.

Based on the description, this research presents a novel method in the development of WO_3/TiO_2-NT/Ti photoanode, where WO_3 and TiO_2-NT are directly integrated in-situ during the anodization process of Ti. This varied significantly from previous investigations where WO_3/TiO_2 composites were typically used as powders rather than photoanodes. The innovative method also introduced a unique strategy for composite semiconductor fabrication in a single-step process. Furthermore, this research was the first to explore hydrogen production within PFC systems, which primarily focused on organic compound degradation and electricity generation.

2. Materials and Method

2.1 Materials

POME was obtained from a palm oil mill in Central Kalimantan, Indonesia. The samples collected were stored at room temperature until use. The POME was filtered using filter paper to remove impurities prior to performance. Ti foil from Shaanxi Yunzhong Metal Technology Co., LTD was used for photoanode fabrication as the substrate and platinum (Pt) electrode. The anodization process included hydrofluoric acid (HF, Merck, 40%), nitric acid (HNO_3, Merck, 65%), and hydrochloric acid (HCl, 37%) to etch the titanium surface. To develop the WO_3/TiO_2-NT/Ti photoanode, ammonium fluoride (NH_4F, Sigma Aldrich) and sodium tungstate dihydrate ($Na_2WO_4{\cdot}2H_2O$, Sigma Aldrich), were used. Glycerol (P&G Chemicals, 98%) and distilled water functioned as a solvent. Potassium hydroxide (KOH, Sigma Aldrich) was used as electrolyte during the PFC performance test. All chemicals were used as received without any further modifications or adjustments.

2.2 Synthesis of WO_3/TiO_2-NT/Ti photoanode

The photoanode synthesis was performed using in-situ anodization. A Ti sheet (99% purity, 0.3 mm thickness, 4 cm x 8 cm) served as the anode, and a Pt (1 mm thickness, 4 cm x 8 cm) as the cathode. Before anodization, the Ti sheet was sanded with 1500-grit sandpaper, cleaned using soap water, and chemically polished in a solution of HF, HNO_3, and H_2O (1:3:46 by volume) for 1 minute, followed by rinsing with distilled water. Anodization was carried out in 150 mL of glycerol electrolyte containing 0.5% NH_4F (1 g), 25% water (50 mL), and a varied amount of Na_2WO_4-$2H_2O$ (0.3 g, 0.5 g., and 0.78 g) under magnetic stirring and a constant voltage of 50 V for 2 hours. This was followed by sonication for 5 minutes in distilled water to remove residual electrolytes remaining from the anodization process Finally, the sample was crystallized through calcination at 550°C for 3 hours. The samples were labeled based on the amount of sodium tungstate used, with 0.3 g, 0.5 g, and 0.78 g $Na_2WO_4{\cdot}2H_2O$ designated as TW3, TW5, and TW7, respectively. Meanwhile, the sample without the addition of $Na_2WO_4{\cdot}2H_2O$ was labeled as TiO_2-NT.

2.3 Characterizations of WO_3/TiO_2-NT/Ti photoanode

The morphology and elemental composition of the synthesized photoanode were analyzed using Field Emission Scanning Electron Microscope (FESEM, Thermo Scientific Quattro S completed with EDS detector) at 10 kV and equipped with Energy Dispersive X-ray spectroscopy (EDX). X-ray Diffraction experiment was performed on an EMPYREAN diffractometer with Cu Kα radiation (λ = 0.15418 Å at 40 kV and 30 mA). The diffraction pattern was recorded from 5° to 89° with a step size of 0.02°. Photoluminescence Microspectrometer Horiba Scientific iHR320 was used with a 325 nm laser beam to provide insights into the electron-hole recombination dynamics. Subsequently, photocurrent was carried out with Palmsense4 Potentiostat in 3 electrode system vs Ag/AgCl and Pt as counter electrode in 0.1 M KOH electrolyte using EPILED LED 410-420 nm as light source. X-ray photoelectron spectroscopy (XPS) was obtained using XPS Kratos AXIS SUPRA PLUS. The optical properties and bandgap values were determined using the Kubelka-Munk functions from UV-Visible Diffuse Reflectance Spectra (UV-Vis DRS, Agilent Cary 60 UV-Vis Spectrophotometer). The data were obtained in the range of 300-600 nm.

2.4 Development of the PFC system setup

The photocatalysis-fuel cell (PFC) system reactor used in this research has internal dimensions of 12 x 12 x 5 cm, with quartz glass windows (10 x 10 cm) on both sides to allow light irradiation. The distance between the photoanode and photocathode was fixed at 2 cm. The light source consisted of 16 pcs 1 W LED lamps EPILEDS (410–420 nm), positioned on all four sides of the photoanode and photocathode. The reactor was made airtight to facilitate hydrogen production monitoring, equipped with copper wires and a 10 Ω resistor connecting the photoanode to Cu_2O/Cu as the photocathode. The PFC system was agitated in moderate stirring without applying external potential. Before the experiment, the reactor was purged with nitrogen gas to remove any oxygen content, ensuring an oxygen-free environment for the process.

2.5 Assessment of the PFC Performance

The PFC was conducted in PFC system reactor filled with 600 mL of POME (initial concentration of 100 mg/L). The electrolyte used was potassium hydroxide (KOH, Sigma Aldrich). The sampling of POME solution was collected at 60-minute intervals during the 240-minute experiment. The COD removal was measured using HR COD vials (HACH) and heated using a block digester (DRB200). The absorbance of the samples was measured using a UV-Vis spectrophotometer (Genesys 10S) at specific wavelengths. Absorbance readings for COD removal were taken at 605 nm and concentration reduction was monitored using Equation (1).

$$\%\ \boldsymbol{COD\ Removal} = \frac{C_0 - C}{C_0} \times 100 \qquad (1)$$

where, C_0 and C denote the concentrations of COD in mg/L (ppm) at the initial time and at specific time intervals, respectively. Electricity generation (voltage) was monitored using a MASTECH MS8229 digital multimeter. The hydrogen production was determined using Gas Chromatography (Shimadzu GC-2014-C114849) equipped with a Molecular Sieve (MS) Hydrogen 5A column, using argon as the carrier gas with a known retention time. Sampling was performed at least in duplicates and the average values were used.

3. Results and Discussion

3.1 X-ray diffraction (XRD) analysis

The crystal structures formed during calcination on crystal size were analyzed using X-ray diffraction (XRD), as shown in Figure 1. The diffraction peaks were observed corresponding to the structural components of the photoanode. The anatase TiO_2 peaks appeared at 2θ = 25.4°, 37.1°, and 48.14°, while WO_3 was visible at 2θ = 55.16°. The average crystallite size of the anatase phase was 28.5 nm and WO_3 was 30.5 nm. The remaining peaks corresponded to Ti, which served as the catalyst substrate. These results were confirmed by the JCPDS data for WO_3 (No. 83-0950) and anatase TiO_2 (No. 21-1272) (W. Li *et al.*, 2014; Momeni & Ghayeb, 2016).

3.2 Photocurrent transient characterization

Photocurrent transient testing was performed using a Palmsens4 potentiostat with a three-electrode configuration. TiO_2 nanotube arrays (TiO_2-NT/Ti) and WO_3/TiO_2-NT/Ti were the working electrodes. Pt and Ag/AgCl were counter and reference electrodes respectively, at a constant potential of 0.5 V in 0.1M KOH solution (Bi *et al.*, 2020). The results showed that WO_3/TiO_2-NT/Ti generated a photocurrent of 0.009, 0.008, and 0.0075 mA/cm² for TW3, TW5, and TW7 respectively under illumination. Meanwhile, TiO_2-NT generated only 0.0061 mA/cm². A 16 W LED light source was used to obtain the results with a wavelength range of 410–420 nm. Figure 2 shows the amperometric I-t curve for TiO_2-NT/Ti and WO_3/TiO_2-NT/Ti.

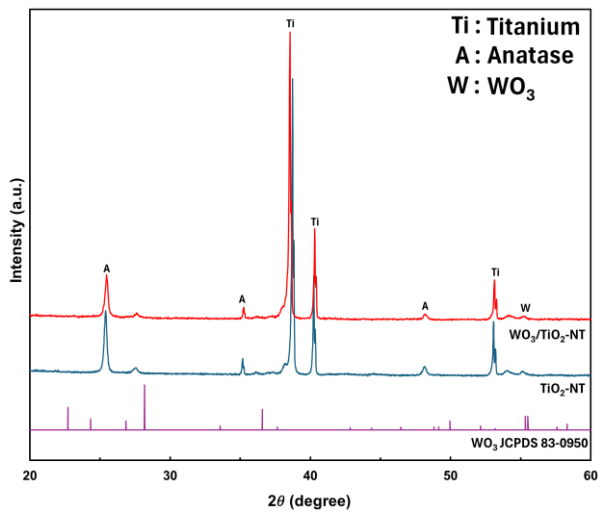

Fig. 1 XRD Pattern of WO_3/TiO_2-NT/Ti and TiO_2-NT/Ti Photoanode

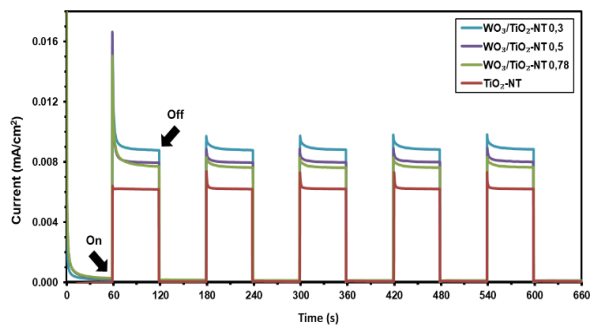

Fig. 2 Amperometric I-t curve of WO_3/TiO_2-NT/Ti and TiO_2-NT/Ti photoanode at 0.5 V bias vs Ag/AgCl

3.3 Photoluminescence spectroscopy

Figure 3 shows the photoluminescence characterization results of the TiO_2-NT/Ti and WO_3/TiO_2-NT/Ti photoanodes. The results showed that nanocomposite formation successfully suppressed the recombination rate of holes and electrons. In

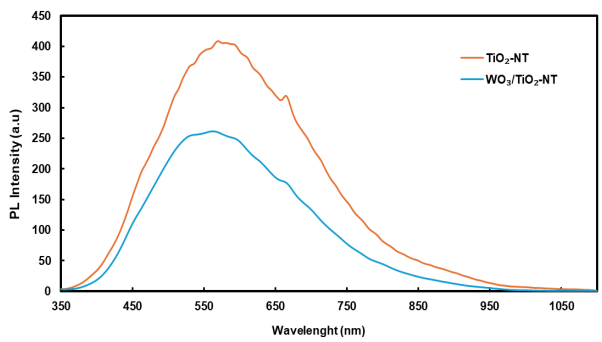

Fig. 3 Photoluminescence spectra of TiO_2-NT/Ti and WO_3/TiO_2-NT/Ti photoanode

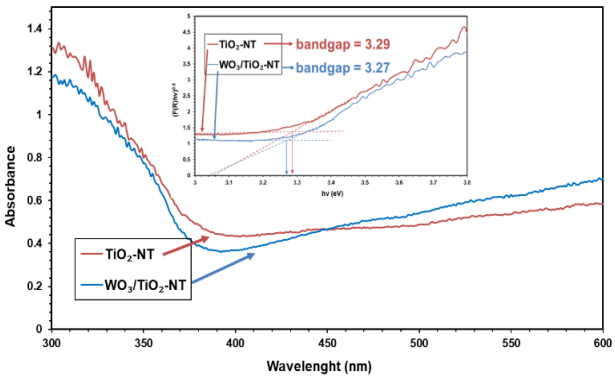

Fig. 4 UV-Vis DRS Spectrum of TiO_2-NT/Ti and WO_3/TiO_2-NT/Ti photoanode

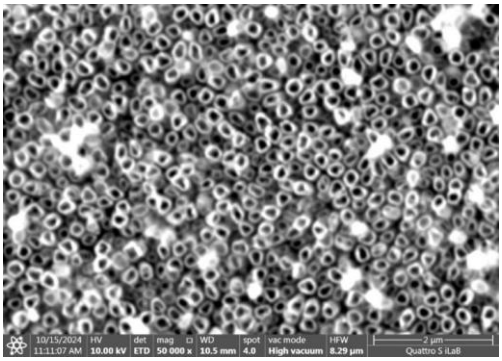

Fig. 5 FESEM image of WO_3/TiO_2-NT/Ti photoanode

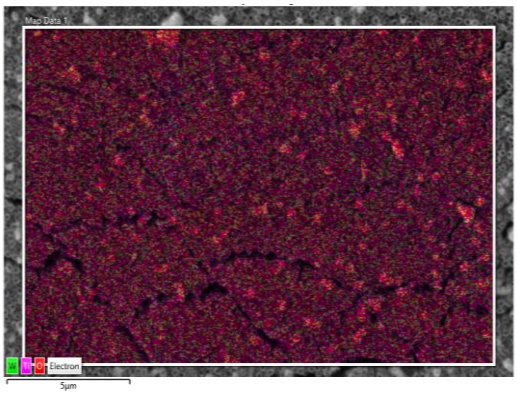

Fig. 6 EDX elemental mapping of WO_3/TiO_2-NT/Ti photoanode

comparison with TiO_2-NT/Ti, photoluminescence peak of the WO_3/TiO_2-NT/Ti nanocomposite was lower suggesting weaker electron transfer. This lower peak showed a reduction in electron-hole recombination, which was desirable for improved photocatalytic performance.

3.4 UV-Vis DRS

The UV-Vis DRS analysis compared the optical properties of TiO_2-NT and the WO_3/TiO_2-NT composite photoanode by evaluating their absorbance spectra and bandgap energies. The absorbance spectra in Figure 4 showed that TiO_2-NT had stronger light absorption in the UV region (300–450 nm), which was a feature of anatase-phase TiO_2 (Sim *et al.*, 2020). However, the introduction of WO_3 into the TiO_2-NT structure caused a decrease in UV absorbance due to modifications in surface properties or increased light scattering (Mokhtarifar *et al.*, 2020). However, WO_3/TiO_2-NT was found to enhance absorbance in the visible-light region (450–600 nm). This showed that the addition of WO_3 improved light-harvesting capabilities in the visible range, which was essential for extending photocatalytic activity (Luo *et al.*, 2013).

Figure 4 shows the Tauc plot derived from the Kubelka-Munk function. The results showed slight narrowing of the bandgap energy (Eg) for WO_3/TiO_2-NT compared to TiO_2-NT. Measurement of TiO_2-NT bandgap was at 3.29 eV, consistent with typical TiO_2 values (Phromma *et al.*, 2020; Ratnawati *et al.*, 2014). Meanwhile, the WO_3/TiO_2-NT composite showed a lower bandgap of 3.27 eV due to WO_3, a semiconductor with 2.7 eV (Djurišić *et al.*, 2020).

The bandgap energy of WO_3/TiO_2-NT/Ti was between TiO_2-NT/Ti (3.28 eV) and WO_3 (2.7 eV). However, the low reduction in bandgap was due to the limited amount of WO_3 loaded onto the TiO_2-NT/Ti, as confirmed by EDX analysis. This bandgap narrowing enhanced the material's ability to absorb visible light, thereby improving photocatalytic potential (He *et al.*, 2022).

3.5 FESEM-EDX

Figure 5 shows the morphology of photoanode based on FESEM analysis, indicating nanotube arrays arranged on the Ti plate's surface with WO_3 loading. The nanotube arrays showed a wide variety of sizes and dimensions. Subsequently, the dimensions were calculated, showing inner diameters between 164 and 194 nm, wall thicknesses from 28 to 37 nm, and heights ranging from 522 to 703 nm. The preserved morphology suggested that the primary factors influencing nanotube dimensional changes were the anodization conditions, such as H_2O content affecting length and fluoride ions impacting diameter. Other influencing factors were voltage, duration, and stirring conditions that affected the electrolyte solution uniformity during anodization (Indira *et al.*, 2015; Lockman *et al.*, 2010).

The EDX analysis of WO_3/TiO_2-NT/Ti confirmed that the TiO_2-NT layer was successfully formed on Ti plate, with WO_3 being composited within the nanotube layer. This result was attributed to the in-situ anodization synthesis method, where $Na_2WO_4 \cdot 2H_2O$ was added as a precursor to the electrolyte during the anodization process. As shown in Figure 6, the nanotube distribution appeared uniform, forming circular structures. The EDX elemental composition by weight was 69.7%, 30.2%, and 0.1% for Ti, O, and W, respectively.

3.6 X-ray photoelectron spectroscopy (XPS)

The X-ray Photoelectron Spectroscopy (XPS) analysis provided a detailed understanding of the surface composition and chemical states in the WO_3/TiO_2/Ti photoanode, as shown in Figure 7. The high-resolution spectrum for Ti 2p showed two distinct peaks at binding energy of 458.43 eV (Ti $2p_{3/2}$) and 464.12 eV (Ti $2p_{1/2}$), confirming the presence of Ti^{4+} in TiO_2. These peaks were consistent with the values reported in the literature for stoichiometric TiO_2, typically observed at 458.5–459 eV and 463.8–464.5 eV, respectively (Mahadik *et al.*, 2023). The absence of peaks near 455 eV showed the complete oxidation of the Ti substrate, distinguishing TiO_2 from metallic titanium (Ti^0), which had a Ti $2p_{3/2}$ peak at 454.5–455 eV (Natu *et al.*, 2021).

The O 1s spectrum was deconvoluted into two peaks, 530.61 eV and 531.77 eV, representing lattice oxygen (O_L) and surface oxygen vacancies or hydroxyl groups (O_V), respectively. The O_L peak at 530.61 eV was attributed to oxygen in TiO_2 and

WO_3, while the O_V peak indicated the presence of surface defects, serving as electron traps and enhancing photocatalytic performance (Y. Wang *et al.*, 2018). The binding energies observed for oxygen bonded to Ti and tungsten were consistent with previously reported values for TiO_2 (529.8–530.5 eV) (Natu *et al.*, 2021) and WO_3 (530.0–530.8 eV) (Mahadik *et al.*, 2023), showing the successful integration of the two oxides. The higher-energy O_V peak at 531.77 eV showed the presence of oxygen vacancies or adsorbed hydroxyl groups, which were essential for improving catalytic activity.

The W 4f spectrum showed two main peaks at 36.96 eV (W $4f_{7/2}$) and 35.13 eV (W $4f_{5/2}$), corresponding to W^{6+} in WO_3. The values were in line with previous reports, where W^{6+} in WO_3 appeared within the range of 36.8–37.2 eV (Mahadik *et al.*, 2023). The absence of additional peaks at lower binding energies associated with reduced tungsten species (e.g., W^{5+} or W^{4+}) confirmed the formation of stoichiometric WO_3 with minimal oxygen vacancies.

The wide survey spectrum confirmed the presence of Ti, W, and O elements, without significant impurities, validating the composition of the photoanode. Compared to pure TiO_2 or WO_3 films, the combination of these two oxides in the composite material offered potential synergistic effects, such as improved charge separation and photocatalytic activity. The observed peaks and binding energies were consistent with previous reports, showing the successful fabrication of a high-quality $WO_3/TiO_2/Ti$ photoanode with minimal surface defects.

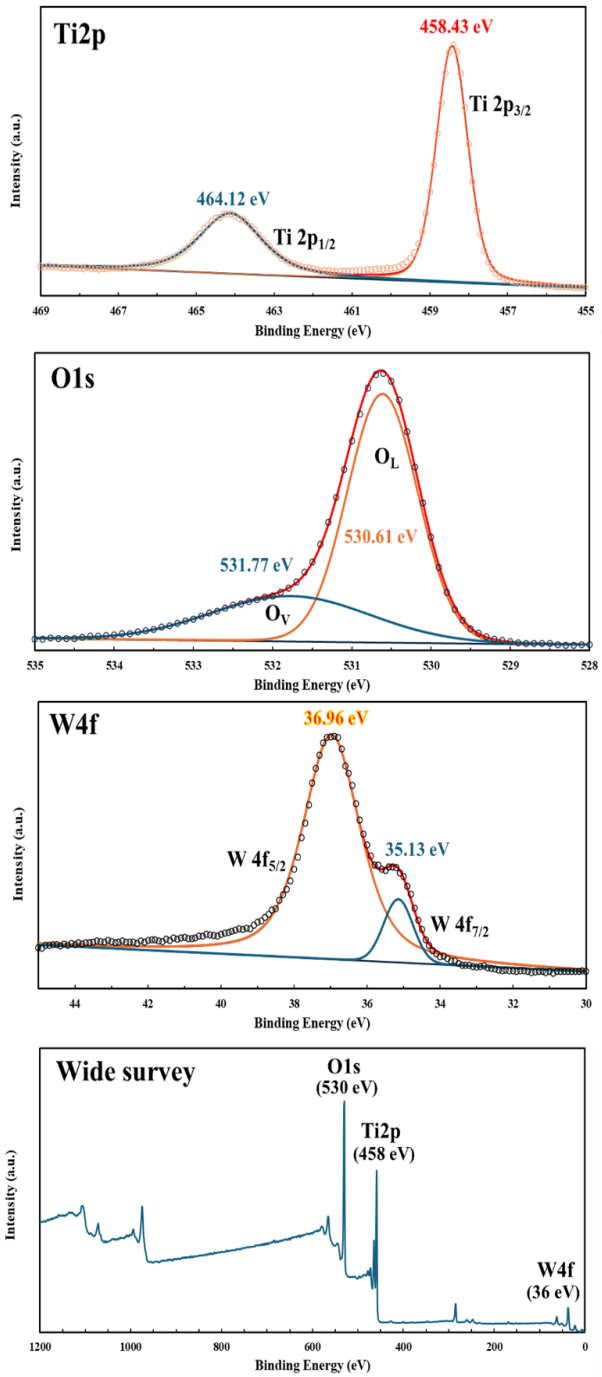

Fig. 7 XPS spectra of Ti2p, O1s, W4f, and wide survey of WO_3/TiO_2-NT/Ti photoanode

3.7 Analysis of performance testing for PFC system

The performance of PFC system using Ti-based photoanodes (TiO_2-NT and WO_3/TiO_2-NT heterojunctions) with three different WO_3 loadings (0.3, 0.5, and 0.78 g) was evaluated for COD degradation, electricity generation, and hydrogen production. A Cu_2O/Cu photocathode was used to enhance the overall system efficiency, with the results shown below.

3.7.1 COD degradation analysis

As presented in Figures 8a and 8b, the PFC system with WO_3/TiO_2-NT photoanode showed better photocatalytic performance compared to PFC with TiO_2-NT photoanode and photocatalysis TiO_2-NT. Among the WO_3/TiO_2-NT samples, the TW3 (0.3 g WO_3) achieved the highest COD removal efficiency of 84% after 240 minutes. In comparison, TW5 (0.5 g WO_3) and TW7 (0.78 g WO_3) achieved COD degradation rates of 64% and 51%, respectively. The TiO_2-NT photoanode showed a moderate COD reduction, while TiO_2-NT photocatalysis

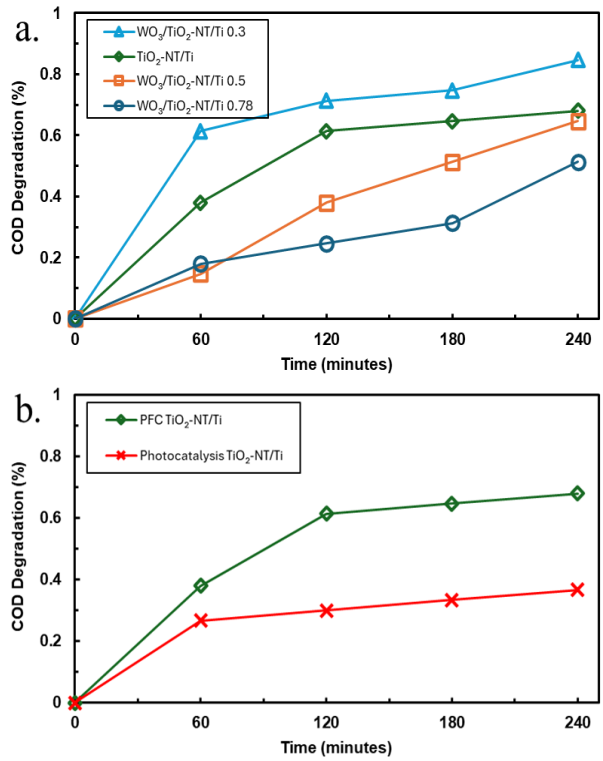

Fig. 8 (a) COD degradation efficiency of WO_3/TiO_2-NT/Ti and TiO_2-NT/Ti photoanode (b) Comparison of PFC TiO_2-NT and photocatalysis TiO_2-NT

(unconnected TiO_2-NT photoanode) performed the least effectively, with only 36% degradation.

The significant improvement observed in the WO_3/TiO_2-NT photoanodes could be attributed to the formation of a heterojunction structure between WO_3 and TiO_2. This heterojunction enhanced light absorption, particularly in the visible spectrum, due to narrow bandgap of WO_3 (2.6–2.8 eV), thereby promoting efficient charge carrier separation by minimizing electron-hole recombination. The photogenerated holes (h^+) in WO_3 effectively oxidized organic compounds in POME, accelerating COD degradation. However, excessive WO_3 loading, as observed in TW5 and TW7, might reduce active surface sites and inhibit light penetration, causing diminished photocatalytic performance (Husein *et al.*, 2024; Pratiwi *et al.*, 2023; Slamet *et al.*, 2022). Kee *et al.*, (2020) also reported the role of concentration composites in improving degradation efficiency.

3.7.2 Electricity Generation Performance

The electricity generation analysis is shown in the current and power density plots (Figures 9a and 9b). The results showed the enhancement achieved by incorporating WO_3 into the TiO_2-NT structure. The TW3 sample showed the highest current density (0.0076 mA/cm²) and power density (0.0375 mW/cm²) after 240 minutes, outperforming TW5, TW7, and TiO_2-NT. The TiO_2-NT photocatalysis system produced negligible electrical output due to the absence of an electron transfer pathway to the Cu_2O/Cu photocathode.

The enhanced current and power generation in WO_3/TiO_2-NT samples was attributed to the synergistic effect of the heterojunction mechanism. Under light irradiation, WO_3 absorbed visible light and generated electrons in its conduction band (CB), which were transferred to the CB of TiO_2 due to the favorable energy band alignment. This process reduced

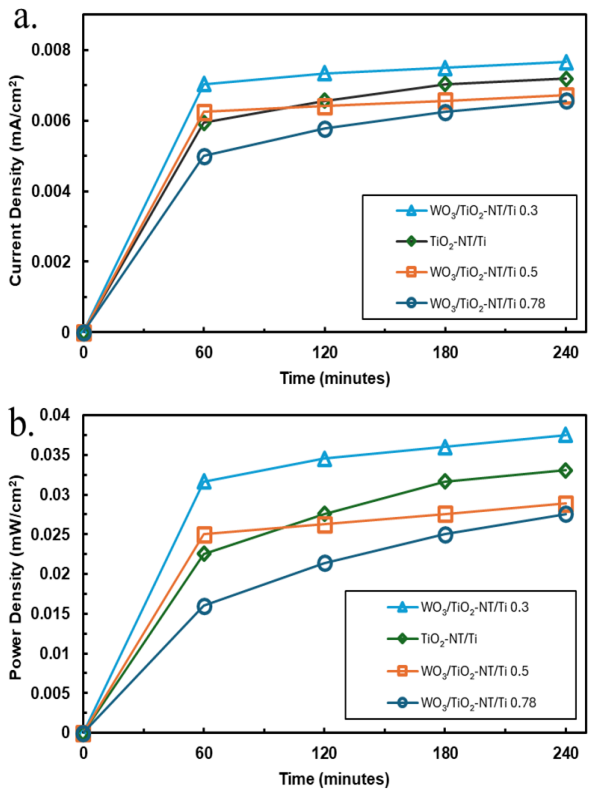

Fig. 9 (a) Current density and (b) power density of WO_3/TiO_2-NT/Ti and TiO_2-NT/Ti photoanode

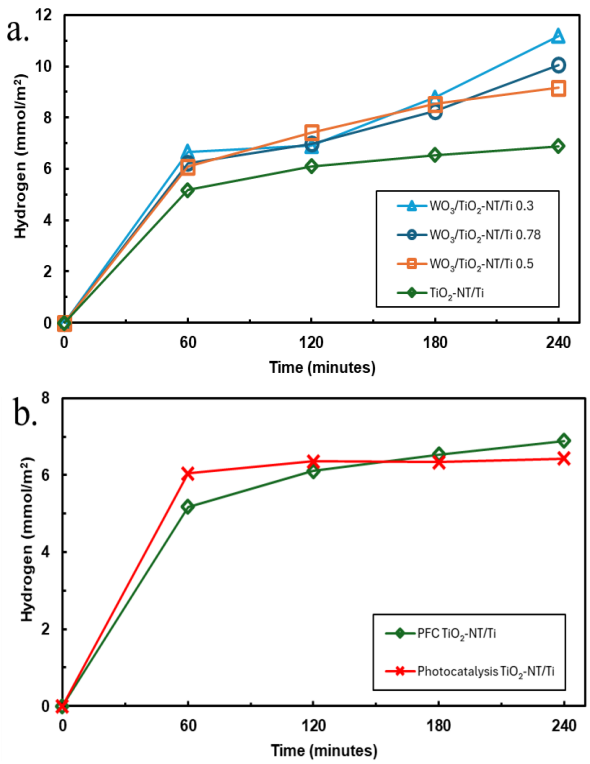

Fig. 10 (a) Hydrogen production of WO_3/TiO_2-NT/Ti and TiO_2-NT/Ti photoanode (b) Hydrogen production of PFC TiO_2-NT and photocatalysis TiO_2-NT

electron-hole recombination, increasing the availability of electrons for transfer to the Cu_2O/Cu photocathode, which contributed to hydrogen evolution and power generation. The optimal WO_3 content in TW3 provided sufficient active sites and maintained efficient light absorption without hindering charge transfer, showing superior performance compared to TW5 and TW7. Similarly, (Kee *et al.*, 2020) emphasized the importance of heterojunctions for improving photocurrent densities in TiO_2-based photoanodes.

3.7.3 Hydrogen Production Analysis

As presented in Figure 10a, the TW3 sample showed the highest cumulative hydrogen generation (11.18 mmol/m²) after 240 minutes, followed by TW7 and TW5. In comparison, the TiO_2-NT photoanode and photocatalysis TiO_2-NT systems generated significantly lower hydrogen yields. The superior hydrogen evolution in TW3 could be attributed to the optimized WO_3 loading (0.3 g), which enhanced visible-light absorption and charge separation efficiency. The mechanism included the excitation of electrons (e^-) in WO_3 under visible light, followed by their transfer to TiO_2-NT and Cu_2O/Cu photocathode. At the photocathode, these electrons drive the hydrogen evolution reaction (HER) through the reduction of protons (H^+):

$$2H^+ + 2e^- \rightarrow H_2 \quad (2)$$

The photogenerated holes in WO_3/TiO_2-NT facilitated the oxidation of organic pollutants, contributing to simultaneous COD degradation. The higher hydrogen production observed in TW3 suggested that 0.3 g WO_3 provided an optimal balance between light absorption, charge separation, and surface reactivity. Excess WO_3 in TW7 and TW5 could function as a light-shielding layer, reducing photocatalytic efficiency (Husein

et al., 2024; Muttaqin *et al.*, 2022; Pratiwi *et al.*, 2023; Yu *et al.*, 2024).

3.7.4 Mechanism of heterojunction WO_3/TiO_2-NT/Ti photoanode

The mechanism of heterojunction formation between TiO_2 and WO_3 significantly influenced the overall performance of COD degradation, electricity generation, and hydrogen production in the PFC system. Based on the experimental findings, the system can adopts two primary heterojunction mechanisms, namely Z-scheme and Type-II based on the WO_3 loading (Z. Wang *et al.*, 2021). These mechanisms determine the efficiency of charge separation, electron-hole recombination rate, and redox potential of the system (Ge *et al.*, 2019). However, we have not yet been able to confirm with certainty which heterojunction mechanism predominantly governs the system.

In the Z-scheme heterojunction, under light irradiation, both WO_3 and TiO_2 are excited to generate electron-hole pairs in their conduction band (CB) and valence band (VB), respectively. The electrons from the conduction band of WO_3 recombine with the holes in the valence band of TiO_2 and excite to the conduction band of TiO_2 which effectively suppresses the charge recombination. This recombination process enables the retention of highly active electrons in the conduction band of TiO_2 and highly oxidizing holes in the valence band of WO_3. In comparison, the valence band WO_3 has a more positive oxidation potential (3.5 V vs. NHE) than TiO_2 (2.9 V vs. NHE) (Djurišić *et al.*, 2020), facilitating efficient oxidation of organic pollutants in POME. Meanwhile, the conduction band electrons of TiO_2 migrate to the Cu_2O photocathode because of the favourable Fermi level arrangement, contributing to the HER and electricity generation (He *et al.*, 2022; Queiroz *et al.*, 2022). This synergistic charge transfer pathway in the Z-scheme mechanism ensures high redox activity and enhanced separation of charge carriers, thereby explaining the superior performance of WO_3/TiO_2-NT/Ti photoanode in COD degradation, current density generation, and hydrogen production (Z. Wang *et al.*, 2021).

For Type-II heterojunction mechanism, the staggered band arrangement between WO_3 and TiO_2 leads to the migration of electrons from the conduction band of TiO_2 to WO_3. Meanwhile, the holes are transferred from the valence band of WO_3 to TiO_2. This mechanism reduces the rate of electron-hole recombination, but the redox potentials of the separated charge carriers are compromised. The electrons in the conduction band of TiO_2, which transfer to the conduction band of WO_3, possess a lower reducing potential compared to those in the Z-scheme mechanism. Similarly, the holes in the valence band of TiO_2 show weaker oxidative potential. The illustration describing the mechanisms occurring in both Type-II and Z-scheme heterojunctions, particularly in the WO_3/TiO_2-NT composite for POME degradation, electricity generation, and hydrogen production, has been provided in Figure 11. Additionally, the schematic also includes the involvement of Cu_2O/Cu as the photocathode in the system.

At the WO_3/TiO_2 interface in Z-scheme, the recombination of less active carriers maximizes the redox ability. This serves as the best option for applications requiring strong oxidative and reductive potentials, such as COD degradation. Meanwhile, the Type-II heterojunction prioritizes charge separation and electron availability. The conduction band of TiO_2 lies slightly lower than WO_3, while the valence band is positioned lower higher. This arrangement drives the direction of charge carrier migration and determines the heterojunction type. In the Z-scheme mechanism, the recombination pathway enables efficient use of the charge carriers' redox potential. Meanwhile, in Type-II mechanism, the spatial separation of electrons and holes reduces recombination but limits their redox power.

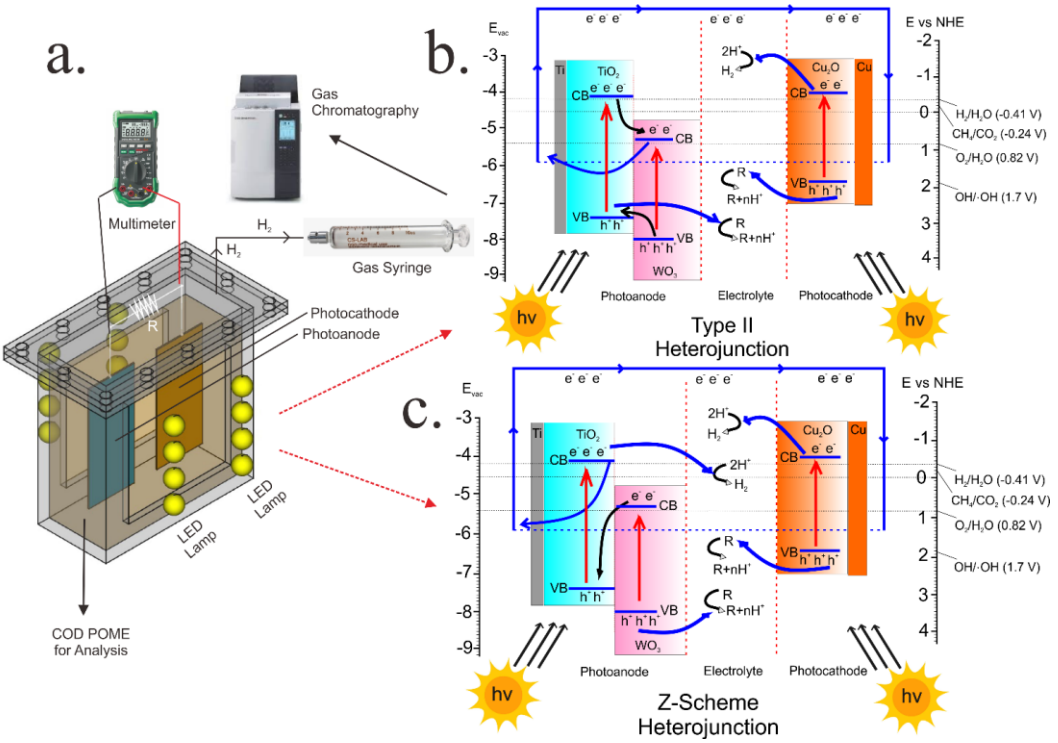

Fig. 11 (a) Schematic design of the photocatalysis-fuel cell reactor system with a WO_3/TiO_2-NT/Ti photoanode and a Cu_2O/Cu photocathode, (b) illustration of the charge transfer mechanism via a type-II heterojunction, and (c) via a Z-scheme heterojunction.

4. Conclusion

In conclusion, this research showed that WO_3/TiO_2-NT/Ti photoanode had excellent performance in PFC system for POME degradation, hydrogen production, and electricity generation. The results showed that TW3 achieved the highest COD degradation of 84% and 11.18 mmol/m² for hydrogen production, TW3 photoanode showed the highest power density of 0.0375 mW/cm², facilitated by efficient electron transfer from WO_3 to the conduction band of TiO_2 and the Cu_2O photocathode. The WO_3/TiO_2-NT/Ti photoanode showed promising properties for integrated photocatalytic and photoelectrochemical applications, offering significant potential for wastewater treatment, clean energy generation, and hydrogen production.

Acknowledgments

This research was funded by the Directorate of Research, Technology, and Community Service, Ministry of Education, Culture, Research, and Technology, Republic of Indonesia (Kemdikbudristek RI). The authors are also grateful to the Indonesia Endowment Fund for Education Agency, Ministry of Finance, Republic of Indonesia (LPDP Kemenkeu RI) for providing the master's scholarship that enabled the first author to complete the master's program in Chemical Engineering. Furthermore, the authors extend their gratitude to the Department of Chemical Engineering, Faculty of Engineering, Universitas Indonesia (FTUI) for providing research facilities during the master's program, as well as to the National Research and Innovation Agency of Indonesia (BRIN), the Forensic Laboratory Center of the Criminal Investigation Agency, Indonesian National Police (PUSLABFOR POLRI), and the Integrated Laboratory and Research Center, Universitas Indonesia (ILRC UI) for facilitating the characterization of the photoanode.

Author Contributions: M.F.B.: Principal researcher responsible for data collection and initial data interpretation. S.H.: Directed research activities, developed research methodology, and performed initial data processing. B.H.S.: Provided feedback on manuscript writing, guided research methods, and assisted in the procurement of materials and equipment. R: Conducted material characterization and contributed to the interpretation of characterization data. S: Provided the initial concept and research ideas, directed the research methodology, and reviewed and revised the manuscript. All authors have read and agreed to the published version of the manuscript.

Funding: This research was funded by the Directorate of Research, Technology, and Community Service, Directorate General of Higher Education, Research, and Technology, Ministry of Education, Culture, Research, and Technology of the Republic of Indonesia, under contract number NKB-963/UN2.RST/HKP.05.00/2024. The authors gratefully acknowledge the financial support that made this research possible.

Conflicts of Interest: The authors declare that there are no conflicts of interest regarding the publication of this paper. All funding and support received have not influenced the design, execution, or conclusions.

References

Alhaji, M. H., Sanaullah, K., Lim, S. F., Khan, A., Hipolito, C. N., Abdullah, M. O., Bhawani, S. A., & Jamil, T. (2016). Photocatalytic treatment technology for palm oil mill effluent (POME) - A review. *Process Safety and Environmental Protection*, *102*, 673–686. https://doi.org/10.1016/j.psep.2016.05.020

Bi, X., Yu, S., Liu, E., Liu, L., Zhang, K., Zang, J., & Zhao, Y. (2020). Construction of g-C_3N_4/TiO_2 nanotube arrays Z-scheme heterojunction to improve visible light catalytic activity. *Colloids and Surfaces A: Physicochemical and Engineering Aspects*, *603*(May), 125193. https://doi.org/10.1016/j.colsurfa.2020.125193

Chen, Q., Li, J., Li, X., Huang, K., Zhou, B., Cai, W., & Shangguan, W. (2012). Visible-Light Responsive Photocatalytic Fuel Cell Based on WO_3/W Photoanode and Cu_2O/Cu Photocathode for Simultaneous Wastewater Treatment and Electricity Generation. *Environmental Science & Technology*, *46*(20), 11451–11458. https://doi.org/10.1021/es302651q

Djurišić, A. B., He, Y., & Ng, A. M. C. (2020). Visible-light photocatalysts: Prospects and challenges. *APL Materials*, *8*(3), 1–24. https://doi.org/10.1063/1.5140497

Ge, J., Zhang, Y., Heo, Y. J., & Park, S. J. (2019). Advanced design and synthesis of composite photocatalysts for the remediation of wastewater: A review. In *Catalysts* (Vol. 9, Issue 2). https://doi.org/10.3390/catal9020122

He, Y., Chen, K., Leung, M. K. H., Zhang, Y., Li, L., Li, G., Xuan, J., & Li, J. (2022). Photocatalytic fuel cell – A review. *Chemical Engineering Journal*, *428*(May 2021). https://doi.org/10.1016/j.cej.2021.131074

Husein, S., Rustamadji, R. R., Pratiwi, R., Dewi, E. L., & Slamet. (2024). Simultaneous tartrazine-tetracycline removal and hydrogen production in the hybrid electrocoagulation-photocatalytic process using g-C_3N_4/TiNTAs. *Communications in Science and Technology*, *9*(1), 46–56. https://doi.org/10.21924/cst.9.1.2024.1308

Indira, K., Mudali, U. K., Nishimura, T., & Rajendran, N. (2015). A Review on TiO_2 Nanotubes: Influence of Anodization Parameters, Formation Mechanism, Properties, Corrosion Behavior, and Biomedical Applications. *Journal of Bio- and Tribo-Corrosion*, *1*(4). https://doi.org/10.1007/s40735-015-0024-x

Kamyab, H., Chelliapan, S., Din, M. F. M., Rezania, S., Khademi, T., & Kumar, A. (2018). Palm Oil Mill Effluent as an Environmental Pollutant. *Palm Oil*. https://doi.org/10.5772/intechopen.75811

Kee, M. W., Lam, S. M., Sin, J. C., Zeng, H., & Mohamed, A. R. (2020). Explicating charge transfer dynamics in anodic TiO_2/ZnO/Zn photocatalytic fuel cell for ameliorated palm oil mill effluent treatment and synchronized energy generation. *Journal of Photochemistry and Photobiology A: Chemistry*, *391*(September 2019), 112353. https://doi.org/10.1016/j.jphotochem.2019.112353

Kustiningsih, I., Pujiastuti, H., Sari, D. K., Rochmat, A., & Slamet. (2023). The Addition of Anthocyanin as a Sensitizer for TiO_2 Nanotubes in a Combined Process of Electrocoagulation and Photocatalysis for Methylene Blue Removal. *Sustainability*, *15*(21), 15384. https://doi.org/10.3390/su152115384

Lee, S. L., Ho, L. N., Ong, S. A., Wong, Y. S., Voon, C. H., Khalik, W. F., Yusoff, N. A., & Nordin, N. (2016). Enhanced electricity generation and degradation of the azo dye Reactive Green 19 in a photocatalytic fuel cell using ZnO/Zn as the photoanode. *Journal of Cleaner Production*, *127*, 579–584. https://doi.org/10.1016/j.jclepro.2016.03.169

Li, J., Li, J., Chen, Q., Bai, J., & Zhou, B. (2013). Converting hazardous organics into clean energy using a solar responsive dual photoelectrode photocatalytic fuel cell. *Journal of Hazardous Materials*, *262*, 304–310. https://doi.org/10.1016/j.jhazmat.2013.08.066

Li, W., Liang, R., Hu, A., Huang, Z., & Zhou, Y. N. (2014). Generation of oxygen vacancies in visible light activated one-dimensional iodine TiO2 photocatalysts. *RSC Advances*, *4*(70), 36959–36966. https://doi.org/10.1039/c4ra04768k

Lianos, P. (2017). Review of recent trends in photoelectrocatalytic conversion of solar energy to electricity and hydrogen. *Applied Catalysis B: Environmental*, *210*, 235–254. https://doi.org/10.1016/j.apcatb.2017.03.067

Lockman, Z., Sreekantan, S., Ismail, S., Schmidt-Mende, L., & MacManus-Driscoll, J. L. (2010). Influence of anodisation voltage on the dimension of titania nanotubes. *Journal of Alloys and Compounds*, *503*(2), 359–364. https://doi.org/10.1016/j.jallcom.2009.12.093

Lui, G., Jiang, G., Fowler, M., Yu, A., & Chen, Z. (2019). A high performance wastewater-fed flow-photocatalytic fuel cell. *Journal of Power Sources*, *425*(June 2018), 69–75. https://doi.org/10.1016/j.jpowsour.2019.03.091

Luo, X., Liu, F., Li, X., Gao, H., & Liu, G. (2013). WO_3/TiO_2 nanocomposites: Salt-ultrasonic assisted hydrothermal synthesis and enhanced photocatalytic activity. *Materials Science in Semiconductor Processing*, *16*(6), 1613–1618. https://doi.org/10.1016/j.mssp.2013.04.005

Madaki, Y. S., & Seng, L. (2013). Pollution Control: How feasible is Zero Discharge Concepts in Malaysia Palm Oil Mills. *American Journal of Engineering Research (AJER)*, *2*(10), 239–252. http://www.ajer.org/papers/v2(10)/ZB210239252.pdf

Mahadik, M. A., Hwang, I. S., Chae, W. S., Lee, H. H., Choi, S. H., Cho, M., & Jang, J. S. (2023). Synergistic role of hydrogen treatment and heterojunction in H-WO_3-x/TiO_2-xNT/Ti foil-based photoanodes for photoelectrochemical wastewater detoxification and antibacterial activity. *Chemosphere*, *318*(January), 137973. https://doi.org/10.1016/j.chemosphere.2023.137973

Mokhtarifar, M., Nguyen, D. T., Diamanti, M. V., Kaveh, R., Asa, M., Sakar, M., Pedeferri, M., & Do, T.-O. (2020). Fabrication of dual-phase TiO_2/WO_3 with post-illumination photocatalytic memory. *New Journal of Chemistry*, *44*(46), 20375–20386. https://doi.org/10.1039/D0NJ04694A

Moksin, N. S. A., Ong, Y. P., Ho, L. N., & Tay, M. G. (2021). Optimization of photocatalytic fuel cells (PFCs) in the treatment of diluted palm oil mill effluent (POME). *Journal of Water Process Engineering*, *40*(January), 1–6. https://doi.org/10.1016/j.jwpe.2020.101880

Momeni, M. M., & Ghayeb, Y. (2016). Preparation of cobalt coated TiO_2 and WO_3-TiO_2 nanotube films via photo-assisted deposition with enhanced photocatalytic activity under visible light illumination. *Ceramics International*, *42*(6), 7014–7022. https://doi.org/10.1016/j.ceramint.2016.01.089

Muttaqin, R., Pratiwi, R., Ratnawati, Dewi, E. L., Ibadurrohman, M., & Slamet. (2022). Degradation of methylene blue-ciprofloxacin and hydrogen production simultaneously using combination of electrocoagulation and photocatalytic process with Fe-TiNTAs. *International Journal of Hydrogen Energy*, *47*(42), 18272–18284. https://doi.org/10.1016/j.ijhydene.2022.04.031

Natu, V., Benchakar, M., Canaff, C., Habrioux, A., Célérier, S., & Barsoum, M. W. (2021). A critical analysis of the X-ray photoelectron spectra of Ti_3C_2Tz MXenes. *Matter*, *4*(4), 1224–1251. https://doi.org/10.1016/j.matt.2021.01.015

Ong, Y. P., Ho, L. N., Ong, S. A., Banjuraizah, J., Ibrahim, A. H., Lee, S. L., & Nordin, N. (2019). A synergistic heterostructured ZnO/$BaTiO_3$ loaded carbon photoanode in photocatalytic fuel cell for degradation of Reactive Red 120 and electricity generation. *Chemosphere*, *219*, 277–285. https://doi.org/10.1016/j.chemosphere.2018.12.004

Phromma, S., Wutikhun, T., Kasamechonchung, P., Eksangsri, T., & Sapcharoenkun, C. (2020). Effect of calcination temperature on photocatalytic activity of synthesized TiO2 nanoparticles via wet ball milling sol-gel method. *Applied Sciences (Switzerland)*, *10*(3). https://doi.org/10.3390/app10030993

Pratiwi, R., Ibadurrohman, M., Dewi, E. L., & Slamet. (2023). A novel approach in the synthesis of CdS/titania nanotubes array nanocomposites to obtain better photocatalyst performance. *Communications in Science and Technology*, *8*(1), 16–24. https://doi.org/10.21924/cst.8.1.2023.1049

Puyol, D., Barry, E. M., Hülsen, T., & Batstone, D. J. (2017). A mechanistic model for anaerobic phototrophs in domestic wastewater applications: Photo-anaerobic model (PAnM). *Water Research*, *116*, 241–253. https://doi.org/10.1016/j.watres.2017.03.022

Queiroz, B. D., Fernandes, J. A., Martins, C. A., & Wender, H. (2022). Photocatalytic fuel cells: From batch to microfluidics. *Journal of Environmental Chemical Engineering*, *10*(3). https://doi.org/10.1016/j.jece.2022.107611

Ratnawati, Gunlazuardi, J., Dewi, E. L., & Slamet. (2014). Effect of $NaBF_4$ addition on the anodic synthesis of TiO_2 nanotube arrays photocatalyst for production of hydrogen from glycerol-water solution. *International Journal of Hydrogen Energy*, *39*(30), 16927–16935. https://doi.org/10.1016/j.ijhydene.2014.07.178

Sim, L. C., Koh, K. S., Leong, K. H., Chin, Y. H., Aziz, A. A., & Saravanan, P. (2020). In situ growth of g-C_3N_4 on TiO_2 nanotube arrays: Construction of heterostructures for improved photocatalysis properties. *Journal of Environmental Chemical Engineering*, *8*(1). https://doi.org/10.1016/j.jece.2019.103611

Slamet, S., Pelawi, L. F., Ibadurrohman, M., Yudianti, R., & Ratnawati. (2022). Simultaneous Decolorization of Tartrazine and Production of H_2 in a Combined Electrocoagulation and Photocatalytic Processes using CuO-TiO_2 Nanotube Arrays: Literature Review and Experiment. *Indonesian Journal of Science and Technology*, *7*(3), 385–404. https://doi.org/10.17509/ijost.v7i3.51315

Tabassum, S., Zhang, Y., & Zhang, Z. (2015). An integrated method for palm oil mill effluent (POME) treatment for achieving zero liquid discharge - A pilot study. In *Journal of Cleaner Production* (Vol. 95). Elsevier Ltd. https://doi.org/10.1016/j.jclepro.2015.02.056

Tan, H. M., Gouwanda, D., & Poh, P. E. (2018). Adaptive neural-fuzzy inference system vs. anaerobic digestion model No.1 for performance prediction of thermophilic anaerobic digestion of palm oil mill effluent. *Process Safety and Environmental Protection*, *117*(1), 92–99. https://doi.org/10.1016/j.psep.2018.04.013

Thanekar, P., Garg, S., & Gogate, P. R. (2020). Hybrid Treatment Strategies Based on Hydrodynamic Cavitation, Advanced Oxidation Processes, and Aerobic Oxidation for Efficient Removal of Naproxen. *Industrial and Engineering Chemistry Research*, *59*(9), 4058–4070. https://doi.org/10.1021/acs.iecr.9b01395

Vasseghian, Y., Khataee, A., Dragoi, E. N., Moradi, M., Nabavifard, S., Oliveri Conti, G., & Mousavi Khaneghah, A. (2020). Pollutants degradation and power generation by photocatalytic fuel cells: A comprehensive review. *Arabian Journal of Chemistry*, *13*(11), 8458–8480. https://doi.org/10.1016/j.arabjc.2020.07.016

Wang, Y., Cai, J., Wu, M., Chen, J., Zhao, W., Tian, Y., Ding, T., Zhang, J., Jiang, Z., & Li, X. (2018). Rational construction of oxygen vacancies onto tungsten trioxide to improve visible light photocatalytic water oxidation reaction. *Applied Catalysis B: Environmental*, *239*(August), 398–407. https://doi.org/10.1016/j.apcatb.2018.08.029

Wang, Z., Lin, Z., Shen, S., Zhong, W., & Cao, S. (2021). Advances in designing heterojunction photocatalytic materials. *Chinese Journal of Catalysis*, *42*(5), 710–730. https://doi.org/10.1016/S1872-2067(20)63698-1

Xia, L., Bai, J., Li, J., Zeng, Q., Li, X., & Zhou, B. (2016). A highly efficient $BiVO_4/WO_3/W$ heterojunction photoanode for visible-light responsive dual photoelectrode photocatalytic fuel cell. *Applied Catalysis B: Environmental*, *183*, 224–230. https://doi.org/10.1016/j.apcatb.2015.10.050

Yu, T., Yang, B., Zhang, R., Yang, C., Arramel, & Jiang, J. (2024). Fabrication of a novel Z-S-scheme photocatalytic fuel cell with the Z-scheme TiO_2/GO/g-C_3N_4 photoanode and S-scheme $BiOAc_1$−xBrx/BiOBr photocathode for TC degradation. *Journal of Materials Science and Technology*, *188*, 11–26. https://doi.org/10.1016/j.jmst.2023.12.004